PanX.4: A Gyrocopter-Borne Six-Band VNIR Multicamera System for Sentinel-2-Aligned Multitemporal Vegetation Monitoring

Alexander Jenal [1], Felix Kröber [2,5], Christopher Frank [3], Lina Krisztian [4], Markus Metz [4], Ribana Roscher [5], Jens Bongartz [1]

[1] Application Center for Machine Learning and Sensor Technologies, University of Applied Sciences Koblenz, Germany – (alexander.jenal, bongartz)@hs-koblenz.de
[2] Institute of Bio- and Geosciences, Forschungszentrum Jülich, Germany – f.kroeber@fz-juelich.de
[3] CISS TDI GmbH, Germany – c.frank@ciss.de
[4] mundialis GmbH & Co. KG, Germany – (krisztian, mmetz)@mundialis.de
[5] Institute of Geodesy and Geoinformation, University of Bonn, Germany – (fkroeber, ribana.roscher)@uni-bonn.de

Keywords: Protected plant communities, shortwave infrared (SWIR), cross-calibration, multisensor co-registration, multispectral.

Abstract

Cross-scale vegetation monitoring of protected European grassland habitats requires sub-meter-resolution imagery that is spectrally consistent with Sentinel-2 time series. We present PanX.4, a gyrocopter-borne six-band VNIR multicamera system designed for spectral alignment with Sentinel-2 MSI bands B02–B06 and B08. The deployed system uses six monochrome 24.6 MP image sensors equipped with bandpass/interference filters spanning 8–130 nm FWHM, integrated into a tri-sensor airborne suite with RGB and VNIR–SWIR payloads on the FlugKit aerial carrier platform. Spectral band adjustment factor (SBAF) analysis quantifying the spectral harmonization quality between PanX.4 and Sentinel-2 was carried out using 1,057 ECOSTRESS spectra. All bands achieved $R^2 > 0.99$; for Sentinel-2A, RMSE values ranged from 3×10^{-4} (B06) to 9.7×10^{-3} (B05). Comparative filter screening identified EO560-20 as the preferred B03 filter and confirmed an approximately 90% RMSE reduction for B06 relative to the legacy BN740 configuration. To deploy the system for multitemporal vegetation monitoring, a multi-year analysis of 86,947 first-mowing observations from 2017 to 2024 reveals substantial interannual variability, supporting a three-window multitemporal acquisition strategy synchronized with management-driven vegetation dynamics at Natura 2000 sites. Together, these results establish the sensor-design and temporal-planning basis for Sentinel-2-harmonized multitemporal airborne monitoring at spatial resolutions two orders of magnitude finer than satellite coverage.

1. Introduction

European habitat monitoring under the EU Habitats Directive relies on Earth observation to complement field surveys, particularly for protected grassland communities, where spatial heterogeneity and management changes challenge repeatable mapping (Vanden Borre et al., 2011). Sentinel-2 MSI (Drusch et al., 2012) provides free multispectral time series with red-edge bands that are informative for canopy chlorophyll, LAI, and vegetation classification (Delegido et al., 2011; Immitzer et al., 2019). However, the 10–20 m ground sampling distance mixes multiple plant communities within pixels in heterogeneous cultural landscapes typical of Central European Natura 2000 sites. For habitat types in which diagnostic indicator species occur in small patches or narrow ecotones, sub-meter reference data are required to (i) validate satellite-derived habitat maps and (ii) support downscaling approaches that translate satellite-scale patterns to management-relevant boundaries.

Recent studies have shown that multitemporal Sentinel-2 data can support the discrimination of Natura 2000 grassland and mountain-vegetation classes when phenology is exploited (Wakulińska and Marcinkowska-Ochtyra, 2020; Tarantino et al., 2021; Marcinkowska-Ochtyra et al., 2023). However, classification remains challenging under heterogeneous, fragmented, or narrow habitats compared with those within a satellite pixel. Airborne hyperspectral or UAV multispectral data improve thematic detail (Jarocińska et al., 2023; Martínez Prentice et al., 2024). Combined satellite–airborne approaches can support upscaling, validation, and transfer of plant-community information from local to landscape scale. This motivates a sensor concept that is spatially fine-grained and spectrally interoperable with Sentinel-2, so that airborne acquisitions can function as harmonized companion data rather than isolated sources. PanX.4 addresses this gap by pursuing sensor-level spectral compatibility with Sentinel-2 in an airborne system designed for repeated habitat-monitoring campaigns.

Although airborne sensors provide the required spatial detail, combining airborne and satellite observations for multitemporal analysis is challenging when spectral response functions differ. Small shifts in the center wavelength or bandwidth alter the measured reflectance around steep vegetation absorption features, critically across the chlorophyll red edge at 700–740 nm, introducing systematic biases into cross-scale model transfer (Helder et al., 2018; Chander et al., 2013). These spectral discrepancies can be corrected through spectral band adjustment factors (SBAF) and linear transfer functions derived from the spectral convolution of reference spectra through respective sensor response functions (Chander et al., 2013). However, SBAF-based harmonization requires that the spectral response of the airborne sensor is precisely characterized. Based on these characterizations, airborne systems can be optimized for Sentinel-2 interoperability. Such cross-sensor spectral harmonization efforts are in line with broader multisensor surface reflectance interoperability work, such as the Harmonized Landsat–Sentinel framework (Claverie et al., 2018).

The current work is part of the KIBI (AI-based Identification and Classification of Protected Plant Communities), an mFUND-funded project (FKZ 19F2276) developing remote sensing and machine-learning workflows for mapping protected plant communities across German Natura 2000 sites. Within KIBI, we developed a modular gyrocopter-borne sensor suite supporting (i) Sentinel-2-compatible multispectral imaging at sub-meter resolution and (ii) multitemporal acquisitions synchronized with phenological phases and management events (e.g., mowing), which drive class separability. The sensor payload was integrated into the FlugKit carrier platform on an AutoGyro MTOsport

(Jenal et al., 2022), enabling flexible repeat flights over target sites. Gyrocopters bridge UAV platforms, which offer high spatial resolution but a limited range and payload, and conventional manned aircraft, which provide wide-area coverage at higher costs and lower flexibility. The AutoGyro MTOsport platform combines payload capacity for a multisensor suite (approximately 10 kg across three payloads) with low-altitude flight (150–800 m AGL), achieving sub-decimeter GSD while covering several square kilometers per sortie, a scale relevant for Natura 2000 site monitoring.

Our work makes four key contributions: (i) We present PanX.4, a six-band VNIR multicamera system that is spectrally aligned with Sentinel-2 and integrated into a tri-sensor airborne suite (VNIR, RGB, and VNIR–SWIR) for coordinated multimodal acquisitions from a gyrocopter platform. (ii) We characterize the system-level spectral response (filter × lens × sensor QE) for all six bands and quantify SBAF harmonization coefficients against S2A, S2B, and S2C using 1,057 measured spectra from the ECOSTRESS spectral library. (iii) We demonstrate the impact of filter selection on spectral harmonization through a comparison of broadband and narrowband replacements. (iv) We analyze first-mowing observations to derive a phenology-synchronized three-window flight timing strategy that provides an operational framework for subsequent multitemporal data acquisition.

2. Methods

2.1 System Architecture and Sensor Integration

The PanX.4 (Figure 1) system comprises six monochrome industrial cameras (24.6 MP) with narrowband interference filters and prime lenses (f = 12 mm). The cameras are arranged in a 2×3 aluminum frame, each dedicated to one Sentinel-2 VNIR band. The six target bands are B02 (Blue, 490 nm), B03 (Green, 560 nm), B04 (Red, 665 nm), B05 (Red Edge 1, 705 nm), B06 (Red Edge 2, 740 nm), and B08 (NIR, 842 nm). Sentinel-2 band B07 (783 nm) is not implemented in the six-channel configuration because the platform is limited to six cameras, and no additional filter offered sufficient benefit within the available mass, volume, and synchronization budget.

Figure 1. Newly developed 6-band VNIR multispectral multicamera system, PanX.4.

PanX.4 integrates into a tri-sensor airborne suite on the FlugKit carrier platform (Jenal et al., 2022) (see Figure 2). The payload includes (i) the PanX.4 VNIR multicamera array for Sentinel-2-aligned multispectral imaging, (ii) a DSLM RGB camera (103 MP, 45 mm lens) providing high-resolution true-color imagery for visual interpretation and surface reconstruction, and (iii) a self-developed six-band VNIR–SWIR imaging system (400–1700 nm, 8 mm lens) extending spectral coverage beyond the VNIR range (Jenal et al., 2024).

The FlugKit carrier provides standardized mechanical interfaces and power distribution for the installed multisensor suite. In the configuration used herein, the gyrocopter platform operates at 600 m above ground level (AGL), yielding GSD values of approximately 13.7 cm for PanX.4, 37.5 cm for the VNIR–SWIR system, and 5.0 cm for the RGB camera. At these altitudes, several square kilometers of coverage can be achieved with standard overlap settings, matching typical Natura 2000 management units.

The PanX.4 architecture is modular at the payload and optical component levels. Individual channels can be equipped with commercial off-the-shelf filters and lenses, allowing system reconfiguration for Sentinel-2 harmonization, red-edge refinement, or alternative vegetation- and moisture-sensitive band settings without redesigning the carrier platform. The standardized interfaces of the FlugKit enable application-specific sensor configurations while maintaining reproducible system integration.

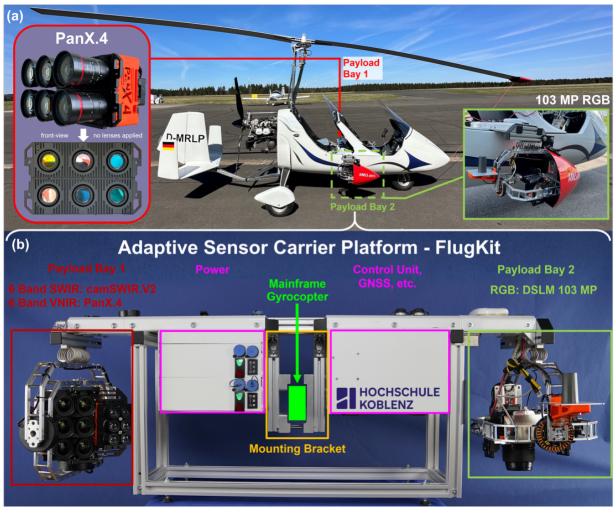

Figure 2. (a) AutoGyro MTOsport with FlugKit carrier platform and the tri-sensor airborne suite. (b) Left: PanX.4 VNIR multicamera array (6 cameras) and six-band VNIR–SWIR imaging system. Right: 103 MP RGB camera. The FlugKit provides standardized mechanical and electrical interfaces for modular payload configurations.

2.2 Spectral Band Selection and Filter Design

Filter selection targeted the maximum spectral overlap with the corresponding Sentinel-2 bands, while meeting the mechanical constraints of the multicamera system (C-mount thread, 25.4 mm clear aperture). Table 1 summarizes the nominal and effective (system-level) specifications of all six bands.

Band	Filter	S2 CWL/ FWHM	Effective CWL/ FWHM	Δλ vs S2	FWHM ratio vs S2
B02	BN490	490/65	491.5/41	+1.5	0.63
B03	EO560-20	560/35	560.0/18	+0.0	0.51
B04	BN660	665/30	656.4/38	-8.6	1.27
B05	FBH700-10	705/15	701.7/9	-3.3	0.60
B06	FBH740-10	740/15	740.1/8	+0.1	0.53
B08	BP850	842/115	860.6/98	+18.6	0.85

Table 1. Nominal Sentinel-2 targets and specifications of deployed PanX.4 system-level bands (center wavelength, CWL, and full width at half maximum, FWHM).

In the deployed configuration, B02 used a MidOpt BN490, B03 used an Edmund Optics EO560-20, B04 used a MidOpt BN660, B05 used a Thorlabs FBH700-10, B06 used a Thorlabs FBH740-10, and B08 used a MidOpt BP850. The system-level effective center wavelengths and bandwidths are listed in Table 1. For the green channel, the initial FBH550-40 candidate and the alternative FBH560-10 were evaluated during filter screening; ECOSTRESS-based SBAF analysis identified EO560-20 as the best-performing B03 option, and thus, it was adopted in the deployed system.

The deployed filter set was obtained by screening off-the-shelf candidates for six Sentinel-2 target bands under spectral and mechanical constraints. For each band, the filters had to match the target center wavelength closely, fit the 25.4 mm clear-aperture/C-mount geometry, and deliver low SBAF residuals after RSR modeling. Most bands had one suitable candidate, whereas B03, B05, and B06 required a head-to-head evaluation of alternatives. The B06 channel illustrates this: both MidOpt BN740 (nom. 50 nm FWHM) and Thorlabs FBH740-10 (nom. 10 nm FWHM) were mechanically compatible; however, BN740 integrated across the red-edge slope and NIR plateau onset, whereas FBH740-10 matched the 15 nm Sentinel-2 B06 band more closely. Therefore, B06 serves as a working comparison example. Figure 3 shows the final PanX.4 band placement relative to Sentinel-2 MSI and highlights the omission of B07 in the six-camera configuration.

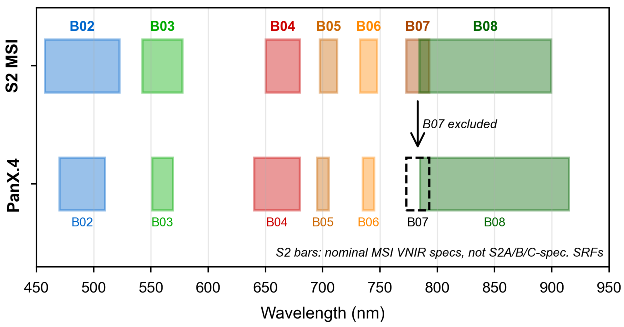

Figure 3. Comparison of band configurations between PanX.4 (bottom) and Sentinel-2 MSI (top). The horizontal bars indicate the center wavelength and FWHM for each band.

2.3 System-Level Spectral Response Characterization

The effective spectral response $R_{sys}(\lambda)$ of each PanX.4 band depends on the combined optical chain of the filter transmission $T_f(\lambda)$, lens transmission $T_l(\lambda)$, and sensor quantum efficiency $QE(\lambda)$. The system-level relative spectral response (RSR) was computed as follows:

$$R_{sys}(\lambda)=T_f(\lambda)\times T_l(\lambda)\times QE(\lambda) \tag{1}$$

Filter transmission curves were resampled using a 1 nm wavelength grid (400–1100 nm) with smooth spline interpolation, whereas lens transmission and sensor QE were resampled using linear interpolation. The normalized RSR was obtained by dividing by the spectral integral to integrate to unity. The effective center wavelength λ_{eff} was defined as the first moment of the normalized RSR, and the effective FWHM was measured as the spectral width where $R_{sys} \geq$ half of the peak value. Filter transmission data were obtained from manufacturer datasheets (Thorlabs, MidOpt, and Edmund Optics), sensor QE from the Sony IMX540 datasheet, and lens transmission from the Kowa LM12FC24M specifications. In deployment, the strongest system-level shift occurred for B08, as the detector QE roll-off truncates the long-wavelength tail of the BP850 filter, whereas the EO560-20 green channel remained centered at the Sentinel-2 B03 position.

This system-level RSR characterization accounts for the wavelength-dependent throughput of the full optical chain, which shifts the effective center wavelengths and modifies bandwidths relative to the nominal filter specifications. In deployment, this effect is strongest for B08 (NIR), where sensor QE decline beyond 850 nm truncates the BP850 filter's long-wavelength tail and narrows the effective passband. The deployed EO560-20 green channel remains centered at 560.0 nm without the short-wavelength shift seen in the preselection candidates.

2.4 Spectral Band Adjustment Factor Analysis

To quantify the spectral harmonization quality between PanX.4 and Sentinel-2, we compute spectral band adjustment factors following Chander et al. (2013) and using an application-specific adaptation by Chen et al. (2018). For a given surface reflectance spectrum $\rho(\lambda)$, the band-integrated reflectance for any sensor is:

$$\rho_{band}=\frac{\int \rho(\lambda)\cdot SRF(\lambda)\, d\lambda}{\int SRF(\lambda)\, d\lambda} \tag{2}$$

The SBAF is defined as a linear relationship between PanX.4 and Sentinel-2 band-integrated reflectances across a diverse set of input spectra:

$$\rho_{S2}=a\cdot\rho_{PanX}+b \tag{3}$$

where a is the slope (ideally 1.0 for a perfect spectral match) and b is the intercept (ideally 0.0). The regression RMSE quantifies the residual spectral mismatch that cannot be corrected by a linear transformation.

For key alternative-filter comparisons at B03, B05, and B06, we evaluated the paired per-spectrum residual differences between candidate filters. We report ΔRMSE as the difference between $RMSE_{alternative}$ and $RMSE_{baseline}$ and quantify the uncertainty with paired bootstrap 95% confidence intervals. Directional robustness was assessed using a paired sign-flip permutation test, and Wilcoxon signed-rank results served as a nonparametric consistency check.

We convolved the spectra through both the PanX.4 system RSR and the Sentinel-2 spectral response functions (S2-SRF version 4.0; European Space Agency, 2024) for all three operational satellites (S2A, S2B, and S2C). The SBAF coefficients were computed for each band–satellite combination via ordinary least squares (OLS) regression.

We used 1,057 measured reflectance spectra from the ECOSTRESS spectral library (Meerdink et al., 2019; Baldridge et al., 2009), which was curated for relevance to Central European monitoring targets. The selection comprised 618 vegetation, 225 rock, 172 mineral, 41 soil, and 1 water spectra, resampled to a common 400–1000 nm grid at 1 nm resolution (minimum wavelength coverage: 420–900 nm). Including geologic spectra alongside vegetation ensures that the SBAF regression captures the full range of spectral slopes and reflectance magnitudes in real monitoring scenarios, following Chen et al. (2018).

The SBAF analysis uses a broad ECOSTRESS subset spanning vegetation and non-vegetation materials. This improves regression generality but means pooled RMSE values reflect a mixed spectral population rather than only grassland canopies. Therefore, we interpret the RMSEs as scene-general harmonization diagnostics and recommend class-stratified reporting for vegetation applications in future.

To assess spectral sensitivity between Sentinel-2 satellites (A/B/C) independently of PanX.4, we convolved the same 1,057

ECOSTRESS spectra through the S2A, S2B, and S2C SRFs and computed pairwise signed relative reflectance differences for each band as

$$\Delta AB = \frac{\rho_{S2B} - \rho_{S2A}}{\rho_{S2A}} \times 100 \quad (4)$$

$$\Delta AC = \frac{\rho_{S2C} - \rho_{S2A}}{\rho_{S2A}} \times 100 \quad (5)$$

$$\Delta BC = \frac{\rho_{S2C} - \rho_{S2B}}{\rho_{S2B}} \times 100 \quad (6)$$

where ρ_{S2A}, ρ_{S2B}, and ρ_{S2C} denote the band-integrated reflectances obtained for the same input spectrum after convolution with the respective Sentinel-2 SRFs. The denominator in each expression is the first satellite in the pair; positive values therefore indicate that the second satellite yields a higher reflectance than the first. Summary statistics are reported as the mean, median, and interquartile range for the full library and separately for the vegetation subset as the application-relevant class for habitat monitoring.

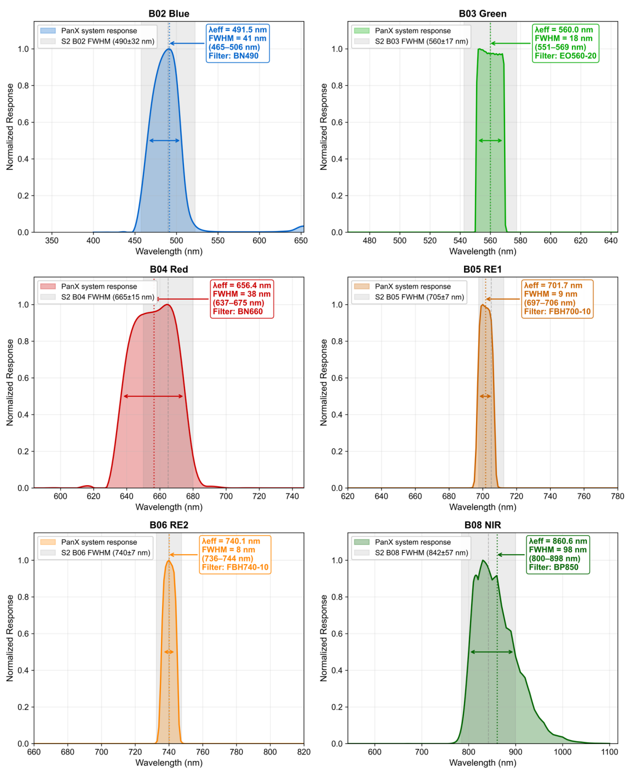

Figure 4. Per-band system spectral response for all six PanX.4 bands. Each panel shows the normalized relative spectral response (RSR, colored fill) with the effective center wavelength (λ_{eff}), FWHM, and filter identification. Grey shaded regions indicate the corresponding Sentinel-2 band FWHM for comparison. The dashed vertical lines indicate the effective center wavelengths.

2.5 Phenology, Mowing Events and Flight Timing

Habitat mapping guidelines define optimal survey periods when diagnostic vegetation patterns are visible and management artifacts (e.g., freshly mown stubbles) are avoided. The Rhineland-Palatinate biotope mapping manual (Kartieranleitung RLP) specifies May–June as optimal for lowland hay meadows (FFH-LRT 6510; MKUEM, 2024). This constraint requires an acquisition concept that accounts for management timing when planning gyrocopter campaigns.

To quantify mowing events for flight planning, we analyzed first-mowing records from the CopGruen[1] mowing detection service for Rhineland-Palatinate FFH grassland habitat types 6210, 6230, 6430, 6510, and 6520 during 2017–2024 (Reinermann et al., 2022; Schwieder et al., 2022; Holtgrave et al., 2023). As the 2024 CopGruen layer remains provisional beta data, its inclusion is noted in interannual plots and interpreted cautiously; however, pooled statistics and operational window derivation use the full 2017–2024 record. For grassland habitat types 6210, 6230, 6510, and 6520, this yielded 95,710 feature-years and 86,947 valid first-mowing observations. LRT 6430 was not interpreted separately because of the low sample size and high uncertainty. Table 3 summarizes the pooled first-mowing timing statistics, and Figure 8 shows habitat-type ECDFs pooled across 2017–2024 that support the phenology-synchronized acquisition windows.

Annual first-mowing events were summarized by the median day-of-year (DOY) for each habitat type and year. The uncertainty in Figure 7 was quantified using percentile bootstrap 95% confidence intervals from 1,000 resamples. For large samples, the bootstrap input was capped at 5,000 observations per group by random subsampling before resampling. For the pooled ECDF in Figure 8, pointwise 95% Wilson score confidence intervals were computed for $I(DOY_{first} \leq x)$ at each day-of-year x. These intervals quantify the uncertainty around cumulative proportion curves; the operational window derivation used the pooled 2017–2024 first-mowing dataset.

3. Results

3.1 System Spectral Response Characterization

Figure 4 shows the per-band system RSR curves for the deployed configuration. The most pronounced system-level deviation occurs for B08, where the combination of the BP850 filter and declining detector QE above 850 nm shifts the effective center wavelength to 860.6 nm and narrows the effective FWHM to 98 nm. After adopting EO560-20, B03 achieves an effective center wavelength of 560.0 nm with an 18 nm FWHM, bringing the green channel into close center-wavelength agreement with Sentinel-2 B03 while remaining spectrally narrower. For the red-edge channels, B05 reaches 701.7 nm with a 9 nm FWHM, and B06 reaches 740.1 nm with an 8 nm FWHM, corresponding to FWHM ratios of 0.60 and 0.53, respectively, relative to Sentinel-2.

PanX.4 Band	Filter	a (slope)	b (offset)	R^2	RMSE
B02 (Blue)	BN490	1.0008	+0.00171	0.9999	0.0024
B03 (Green)	EO560-20	1.0015	−0.00177	1.0000	0.0015
B04 (Red)	BN660	1.0065	−0.00252	0.9997	0.0041
B05 (RE1)	FBH700-10	0.9800	+0.01668	0.9981	0.0097
B06 (RE2)	FBH740-10	1.0001	+0.00017	1.0000	0.0003
B08 (NIR)	BP850	1.0018	−0.00194	0.9993	0.0057

Table 2. Linear SBAF coefficients for the deployed PanX.4 configuration against Sentinel-2A, derived from 1,057 ECOSTRESS spectra. The corresponding S2B and S2C coefficients follow the same band ranking; the largest unit-to-unit sensitivity occurs at B05 and is discussed in Section 3.4.

[1] https://offenland.community.code-de.org/?id=1

https://doi.org/10.5194/isprs-archives-XLIX-B1-2026-93-2026 |

For the narrowband red-edge channels, the system RSR closely matches the filter specifications. B05 (Red Edge 1) reaches an effective center wavelength of 701.7 nm (target: 705 nm, $\Delta\lambda = -3.3$ nm) with a 9 nm FWHM, and B06 (Red Edge 2) reaches 740.1 nm (target: 740 nm, $\Delta\lambda = +0.1$ nm) with an 8 nm FWHM. Both red-edge bands are narrower than their Sentinel-2 counterparts (15 nm FWHM), with FWHM ratios of 0.60 and 0.53, respectively.

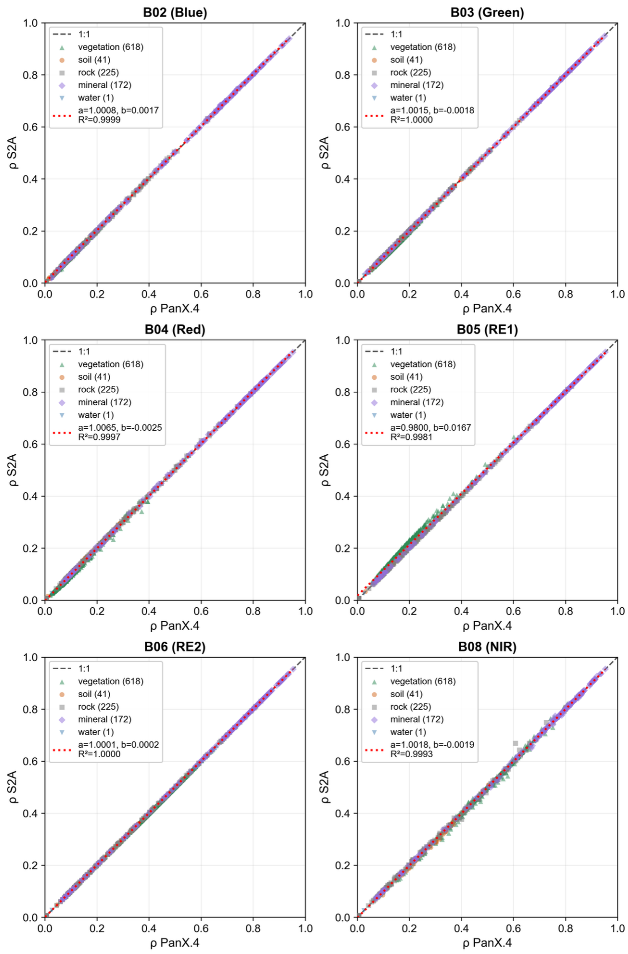

Figure 5. SBAF scatter plots for all six PanX.4 bands against S2A. Each panel shows 1,057 ECOSTRESS spectra color-coded by surface class: vegetation, soil, rock, mineral, and water (distinct marker shapes). Red line: OLS regression (SBAF); dashed gray line: 1:1 reference. Regression statistics are annotated.

3.2 SBAF Harmonization Quality

Table 2 lists the S2A SBAF coefficients for the deployed configuration. The corresponding S2B and S2C coefficient sets are not shown here. Section 3.4 discusses the underlying inter-satellite SRF sensitivity that motivates satellite-specific SBAF parameterization. All S2A regressions achieved $R^2 > 0.99$, confirming that the linear SBAF model captured the spectral response differences well for the ECOSTRESS spectral set. The slopes were closest to unity for B02, B03, B06, and B08, but the residual mismatch remained band-dependent, with B05 and B08 showing the largest RMSE.

Figure 5 shows SBAF scatter plots for all six bands against S2A. The scatter reveals meaningful patterns: vegetation spectra (triangles) cluster in low-reflectance regions for visible bands (B02–B04) due to chlorophyll absorption, whereas soil and mineral spectra (circles) span a wider reflectance range. In NIR bands (B06, B08), vegetation and non-vegetation spectra are clearly separated along the reflectance axis.

B05 (Red Edge 1) shows the largest RMSE among bands, due to its position on the steep portion of the vegetation red edge, where small differences in filter width and center wavelength are amplified by the large reflectance gradient (≈0.4 reflectance change over 50 nm). This sensitivity is an inherent limitation of narrowband red-edge sensing and is not unique to PanX.4; inter-satellite spectral differences between S2A, S2B, and S2C also produced the largest reflectance biases at this position (Section 3.4).

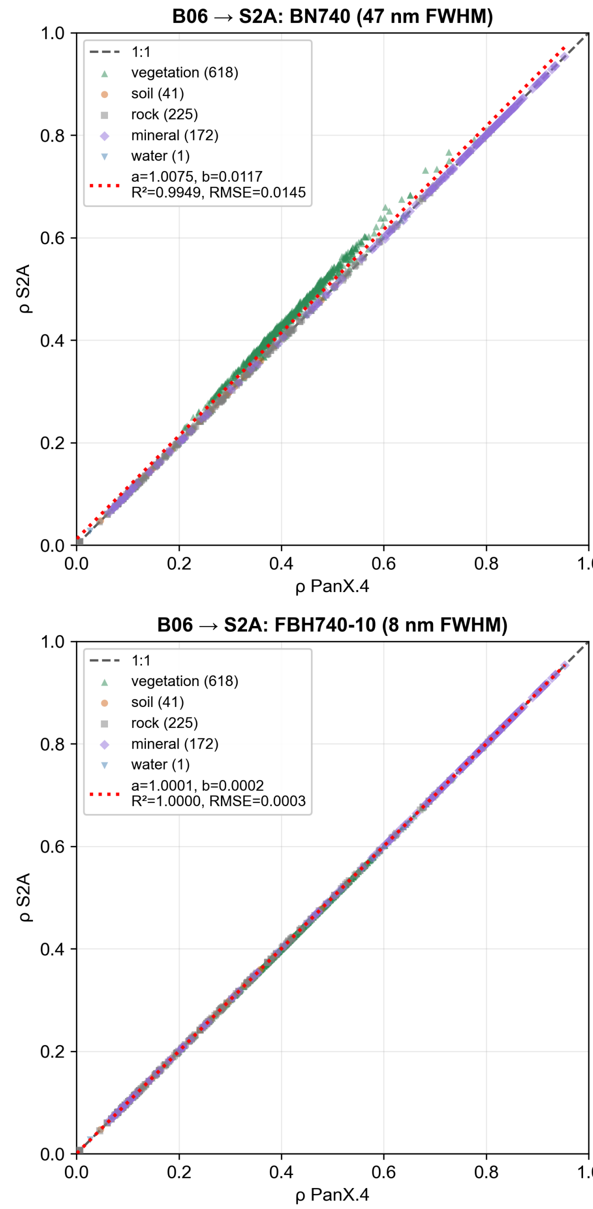

Figure 6. Head-to-head SBAF comparison for PanX.4 B06 against Sentinel-2A using the legacy BN740 broadband filter (top; 47 nm FWHM) and the deployed FBH740-10 narrowband filter (bottom; 8 nm FWHM). The narrower filter aligns much more closely with Sentinel-2 B06. Across S2A/S2B/S2C, the mean RMSE decreases from 0.0139 to 0.0013, corresponding to a reduction of approximately 90 %.

For key alternative-filter comparisons, paired per-spectrum inference confirmed the ECOSTRESS-based ranking: EO560-20 outperformed FBH550-40 for B03 (ΔRMSE = −0.00356, bootstrap 95% CI [−0.00379, −0.00333], permutation $p < 0.001$), EO700-19 underperformed FBH700-10 for B05 (ΔRMSE = +0.00575, 95% CI [+0.00556, +0.00593], $p < 0.001$), and FBH740-10 strongly outperformed the legacy BN740 filter for B06 (ΔRMSE = −0.01239, 95% CI [−0.01256, −0.01223], $p < 0.001$). These results justify the filter choices for all three comparison bands.

3.3 Exemplary Filter Screening: B06 BN740 vs. FBH740-10

Alternative-filter screening was performed for the PanX.4 targets under spectral and mechanical constraints. Candidate filters were required to be compatible with a C-mount/25.4 mm optical geometry while minimizing SBAF residuals after RSR modeling. Head-to-head comparisons were required for B03, B05, and B06, with B06 providing the clearest example of configuration selection. Initially, PanX.4 used a BN740 filter with a 47 nm FWHM for B06 (Red Edge 2), exceeding the 15 nm bandwidth of Sentinel-2 B06. The deployed FBH740-10 (8 nm FWHM) was evaluated as a narrower alternative compatible with the final setup. Figure 6 shows a head-to-head SBAF comparison for this screening case.

Using the ECOSTRESS-based SBAF analysis, the BN740 configuration yielded a mean RMSE of 0.0139 across S2A/S2B/S2C (S2A: 0.0145, S2B: 0.0119, S2C: 0.0152), whereas FBH740-10 reduced the mean RMSE to 0.0013 (S2A: 0.0003, S2B: 0.0025, S2C: 0.0010), representing approximately a 90% reduction. The BN740 passband integrates reflectance across the red-edge slope and NIR plateau onset, blending distinct regions into a single measurement, thereby producing a bias relative to Sentinel-2 B06. FBH740-10 better matches the Sentinel-2 target, thereby reducing residual mismatch. With ECOSTRESS-based comparisons for B03 and B05, this B06 example demonstrates the screening logic for the final filter set. for clarity.

3.4 Inter-Satellite Spectral Sensitivity

Manufacturing tolerances between Sentinel-2 satellites create band-dependent spectral response differences that affect band-integrated reflectance values. Using 1,057 ECOSTRESS spectra from the SBAF analysis, we quantified inter-satellite reflectance differences for all PanX.4 target bands. B05 (Red Edge 1) showed the strongest unit-to-unit sensitivity, with median relative differences of −0.91% for S2A→S2B, +8.72% for S2A→S2C, and +9.62% for S2B→S2C. Outside of B05, the largest difference occurred at B02 for S2A→S2C (median −1.50%), while B03, B04, B06, and B08 remained smaller.

For vegetation data ($n = 618$), which are most relevant for habitat monitoring, this ranking became more pronounced. B05 showed median differences of −1.38% (S2A→S2B), +14.72% (S2A→S2C), and +16.33% (S2B→S2C), with interquartile ranges of +12.61% to +16.56% and +14.02% to +18.39% for the latter comparisons. B06 was the next most sensitive red-edge band, but with smaller magnitudes (median: −1.12%, +0.30%, and +1.43%), while B08 remained insensitive (<0.05% median across pairs). These results confirm that the red-edge region, particularly B05, is sensitive to SRF differences between Sentinel-2 units. For cross-scale vegetation monitoring, when combining PanX.4 imagery with Sentinel-2 time series, SBAF coefficients should be parameterized for the specific satellite unit (S2A, S2B, or S2C) of each overpass. Unit-averaged coefficients would leave systematic biases, especially for B05-based vegetation metrics and classification features.

3.5 Phenology, Mowing Events and Flight Timing

The multi-year CopGruen analysis reveals clear habitat-type-specific differences in first-mowing timing and substantial interannual variability (Figure 7). In the pooled 2017–2024 record, lowland hay meadows (LRT 6510) are mown earliest (Q25: 11 Jun; median: 25 Jun; Q75: 18 Jul), semi-natural dry grasslands (LRT 6210) and mountain hay meadows (LRT 6520) follow shortly afterwards (6210 median: 26 Jun; 6520 median: 27 Jun), and Nardus grasslands (LRT 6230) are latest (Q25: 22 Jun; median: 18 Jul; Q75: 31 Jul). This ranking is robust in the pooled data, but annual medians still shift markedly between years, which argues against deriving operational windows from a single campaign year alone. Figure 7 shows these annual median first-mowing dates explicitly; the bootstrap 95% confidence intervals quantify uncertainty around the annual medians and make the interannual variability transparent.

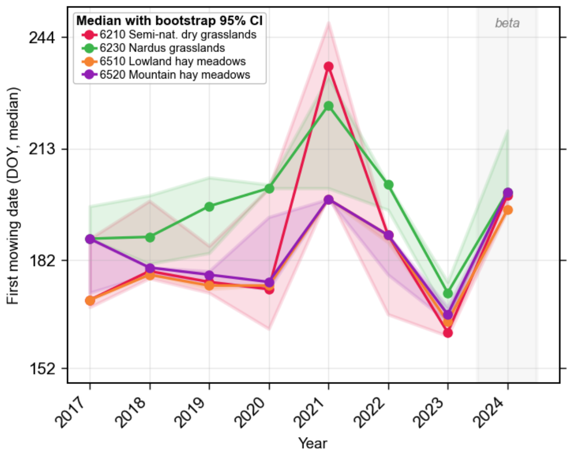

Figure 7. Interannual variation in the median first-mowing day of year (DOY) by FFH habitat type in the CopGruen record. Lines show annual medians; shaded bands indicate bootstrap 95% confidence intervals. The shaded 2024 segment indicates provisional beta data and is shown separately.

Table 3 summarizes the pooled first-mowing timing statistics for the interpreted habitat types. Based on the pooled 2017–2024 empirical cumulative distribution function (ECDF) of first mowing (Figure 8) and the Kartieranleitung RLP survey constraint for hay-meadow mapping, we define three operational acquisition windows. First, a pre-mowing window in May to early June captures peak canopy development before widespread management; in the pooled record, only 18.4% of first mowing events occur by June 1, but early-managed 6510 scenes should be prioritized before May ends. Second, a post-regrowth window in late July to August targets vegetation recovery after the main mowing pulse; the pooled median first mowing date is June 26, and over 90% of first mowing events occur by August 1. Third, a senescence window in September to early October captures late-season structural and moisture differences after the first-cut phase. The pointwise Wilson 95% confidence bands around the ECDF curves show uncertainty in cumulative threshold crossings used for window placement.

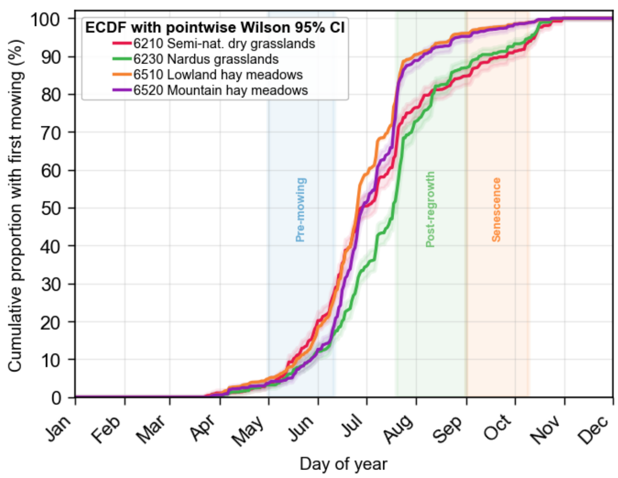

Figure 8. Empirical cumulative distribution function (ECDF) of first-mowing dates by FFH habitat type based on pooled CopGruen feature-year records from 2017 to 2024. Curves show the cumulative share of features with first mowing for each day of the year; shaded bands indicate pointwise 95% Wilson confidence intervals. The figure provides the empirical basis for defining the pre-mowing, post-regrowth, and senescence acquisition windows

The derived multitemporal acquisition strategy aligns with previous studies, confirming that acquisition timing significantly determines habitat separability. Bradter et al. (2020) showed for grass-dominated habitats that classification accuracy varies seasonally and peaks near maximum canopy development as covered by our first acquisition window. Rapinel et al. (2019) and Marcinkowska-Ochtyra et al. (2023) explicitly demonstrate the benefit of multitemporal data for classification of grassland habitats. This supports our three-window acquisition design compared with a single midsummer acquisition.

FFH LRT	n	Q25	Median	Q75
6210	952	09 Jun	26 Jun	26 Jul
6230	918	22 Jun	18 Jul	31 Jul
6510	83,973	11 Jun	25 Jun	18 Jul
6520	1,104	16 Jun	27 Jun	18 Jul

Table 3. Pooled first-mowing timing statistics for interpreted FFH grassland habitat types from the CopGruen record in Rhineland-Palatinate (2017–2024). Values represent date-derived first-mowing observations. LRT 6430 is not interpreted separately because of the low sample size and high uncertainty.

4. Discussion

4.1 Spectral Harmonization Performance

The SBAF analysis showed high linear harmonization quality across all six VNIR bands, with $R^2 > 0.99$. For the deployed configuration, four bands (B02, B03, B04, and B06) achieved S2A RMSE reflectance values below 0.005 units, whereas B05 and B08 remained the largest residual-mismatch bands. B06 provided the strongest match after replacing BN740 with FBH740-10, reaching a near-unity slope and S2A RMSE of 3×10^{-4}. B05 remained the most challenging band owing to the steep red-edge gradient, and B08 was usable but not among the best-matched bands.

The B05 (Red Edge 1) band remains the primary spectral challenge, showing the highest RMSE across the deployed configurations. This result is due to the steep reflectance gradient across the red edge, where the −3.3 nm effective center-wavelength offset between PanX.4 (701.7 nm) and Sentinel-2 (705 nm) maps to a measurable reflectance difference for vegetation targets. This sensitivity is not unique to PanX.4; the ECOSTRESS-based inter-satellite analysis shows that B05 is the most unit-sensitive Sentinel-2 band, with median S2A→S2C differences of +8.72% across the full library and +14.72% for vegetation spectra. The residual difficulty at B05 reflects the intrinsic sensitivity of this spectral position to small SRF shifts between satellite units, not only the airborne filter design. Future iterations could investigate filters centered closer to 705 nm to reduce the PanX.4-side contribution to this effect.
A methodological consideration concerns the spectral library used for SBAF derivation. Although the 1,057 ECOSTRESS spectra provide a diverse basis, they include a substantial proportion of geologic materials (37.6% rock-and-mineral spectra) that may not be representative of Central European grassland monitoring targets. Accordingly, the pooled RMSE values reported herein should be interpreted as scene-general harmonization diagnostics rather than canopy-specific performance estimates; vegetation-only or class-weighted reporting would be a logical next step.

4.2 System Design Considerations

The multicamera approach offers advantages over alternative multispectral sensor architectures. Compared with sequential acquisition systems, it enables simultaneous band capture and avoids motion-induced interband timing offsets. Compared with mosaic-filter snapshot systems, it preserves the native spatial resolution of each spectral channel. The trade-off is greater hardware complexity and the need for rigorous inter-camera geometric calibration.
Tri-sensor integration provides three complementary data streams for habitat monitoring: PanX.4 delivers spectrally harmonized multispectral data for cross-scale comparison with Sentinel-2 time series, the RGB camera provides ultra-high-resolution imagery for structural analysis and photogrammetric products, and the six-band VNIR–SWIR imaging system extends coverage into longer wavelengths for moisture- and material-sensitive analyses. This multimode architecture addresses habitat-monitoring workflows in which different tasks benefit from different spatial–spectral trade-offs.

4.3 Implications for Habitat Monitoring

The practical relevance of spectral harmonization extends beyond the PanX.4 system. Protected area managers increasingly face the challenge of integrating heterogeneous remote sensing data into coherent monitoring programs (Vanden Borre et al., 2011). By designing an airborne system spectrally aligned with the operational satellite baseline and deriving band-specific SBAF correction functions, we establish the basis for a direct comparison of airborne and satellite vegetation indices while minimizing the effects of spectral response differences. This is particularly important for phenology-sensitive indices involving red-edge bands (e.g., NDRE, CIre), where spectral mismatches can produce systematic biases.
4's scientific value lies in enabling a traceable cross-scale observation chain from Sentinel-2 time series to management-scale habitat delineation. Spectrally harmonized airborne imagery can serve as high-resolution reference data for validating habitat maps, refining habitat boundaries, updating management compartments and zoning units, and prioritizing field visits in

protected areas. This is particularly relevant for Natura 2000 monitoring, where ecological units are smaller than a Sentinel-2 pixel, or where mowing and regrowth create short-lived states detectable spectrally but difficult to localize in satellite imagery alone (Vanden Borre et al., 2011; Jarocińska et al., 2023; Martínez Prentice et al., 2024).

The three-window flight timing strategy based on mowing phenology data provides a transferable framework adaptable to other European Natura 2000 sites with managed grassland habitats. The mowing statistics presented herein are specific to the Rhineland-Palatinate study region and require recalibration for areas with different climatic conditions or management regimes. The CopGruen mowing detection service, as a national-scale operational product, could support this adaptation for other German federal states.

4.4 Limitations

Several limitations should be noted. First, RSR characterization relies on manufacturer-provided spectral data for sensor QE and lens transmission rather than independent laboratory measurements of the assembled system. Although standard practice for multicamera design, independent verification would strengthen spectral characterization traceability. Second, the SBAF analysis uses spectral convolution of library spectra without incorporating atmospheric effects, adjacency effects, or BRDF variations that influence airborne-to-satellite comparisons. These factors will be addressed in future work using in-flight validation data. Third, the system excludes the Sentinel-2 band B07 (783 nm) owing to hardware constraints, limiting the computation of vegetation indices that require complete red-edge coverage (e.g., three-band red-edge NDVI).

5. Conclusions and Outlook

We present PanX.4, a six-band VNIR multicamera system for spectral harmonization with Sentinel-2 MSI. System-level spectral characterization shows close center-wavelength agreement for B02–B06, whereas B08 exhibits a larger effective shift to 860.6 nm as the detector QE roll-off truncates the long-wavelength wing of the BP850 filter. The effective FWHM ratios span 0.51–1.27 across the band set. SBAF analysis using 1,057 ECOSTRESS spectra confirms high linear harmonization quality ($R^2 > 0.99$) across all bands and Sentinel-2 satellites. Replacing B06 from the 47 nm BN740 filter with the 8 nm FBH740-10 filter reduced SBAF RMSE by 90%, demonstrating that filter selection is critical for Sentinel-2-aligned airborne systems.

The band-specific system response shows exact center-wavelength agreement for the B03 and B06 channels, moderate offsets for the B02, B04, and B05 channels, and a larger effective shift for the B08 channel because of the broadband BP850 filter and detector QE roll-off. Practical interoperability should be evaluated based on band-specific SBAF performance rather than center wavelength alone.

This study reports on sensor design, system-level spectral characterization, SBAF-based harmonization assessment, and temporal acquisition planning; however, it does not report airborne image products from PanX.4. Future work will focus on (i) airborne radiometric and spectral validation against ground reference spectra and Sentinel-2 overpasses, (ii) operational deployment over Natura 2000 sites with three-window temporal coverage, and (iii) development of cross-scale vegetation classification workflows leveraging spectral consistency between PanX.4 and Sentinel-2 for model transfer.

Acknowledgements

This work was funded by the mFUND program (project KIBI, FKZ 19F2276) of the German Federal Ministry for Digital and Transport (BMDV).

References

Baldridge, A.M., Hook, S.J., Grove, C.I., Rivera, G., 2009. The ASTER spectral library version 2.0. *Remote Sensing of Environment*, 113(4), 711–715, doi.org/10.1016/j.rse.2008.11.007.

Bradter, U., O'Connell, J., Kunin, W. E., Boffey, C. W. H., Ellis, R. J., & Benton, T. G., 2020. Classifying grass-dominated habitats from remotely sensed data: The influence of spectral resolution, acquisition time and the vegetation classification system on accuracy and thematic resolution. *Science of The Total Environment*, 711, 134584, doi.org/10.1016/j.scitotenv.2019.134584.

Chander, G., Mishra, N., Helder, D.L., Aaron, D.B., Angal, A., Choi, T., Xiong, X., Doelling, D.R., 2013. Applications of Spectral Band Adjustment Factors (SBAF) for Cross-Calibration. *IEEE Transactions on Geoscience and Remote Sensing*, 51(3), 1267–1281, doi.org/10.1109/TGRS.2012.2228007.

Chen, F., Song, Y., Zhu, S., Li, J., Wang, C., Zhu, X., 2018. Preliminary Comparison of the Multispectral Cameras Onboard UAV Platform for Environment Monitoring. In: 2018 26th International Conference on Geoinformatics, pp. 1–4, doi.org/10.1109/GEOINFORMATICS.2018.8557041.

Claverie, M., Ju, J., Masek, J. G., Dungan, J. L., Vermote, E. F., Roger, J.-C., Skakun, S. V., Justice, C., 2018. The Harmonized Landsat and Sentinel-2 surface reflectance data set. *Remote Sensing of Environment*, 219, 145–161, doi.org/10.1016/j.rse.2018.09.002.

Delegido, J., Verrelst, J., Alonso, L., Moreno, J., 2011. Evaluation of Sentinel-2 Red-Edge Bands for Empirical Estimation of Green LAI and Chlorophyll Content. *Sensors*, 11(7), 7063–7081, https://doi.org/10.3390/s110707063.

Drusch, M., Del Bello, U., Carlier, S., Colin, O., Fernandez, V., Gascon, F., Hoersch, B., Isola, C., Laberinti, P., Martimort, P., Meygret, A., Spoto, F., Sy, O., Marchese, F., Bargellini, P., 2012. Sentinel-2: ESA's Optical High-Resolution Mission for GMES Operational Services. *Remote Sensing of Environment*, The Sentinel Missions - New Opportunities for Science, 120, 25–36, doi.org/10.1016/j.rse.2011.11.026.

European Space Agency, 2024. Sentinel-2 Spectral Response Functions (S2-SRF), Version 4.0. Available online: https://sentiwiki.copernicus.eu/, accessed: 10 Nov. 2025.

Helder, D., Markham, B., Morfitt, R., Storey, J., Barsi, J., Gascon, F., Clerc, S., LaFrance, B., Masek, J., Roy, D.P., Lewis, A., Pahlevan, N., 2018. Observations and Recommendations for the Calibration of Landsat 8 OLI and Sentinel 2 MSI for Improved Data Interoperability. Remote Sensing, 10(9), 1340, doi.org/10.3390/rs10091340.

Holtgrave, A.-K., Lobert, F., Erasmi, S., Röder, N., Kleinschmit, B., 2023. Grassland mowing event detection using combined optical, SAR, and weather time series. *Remote Sensing of Environment*, 295, 113680, doi.org/10.1016/j.rse.2023.113680.

Immitzer, M., Neuwirth, M., Böck, S., Brenner, H., Vuolo, F., Atzberger, C., 2019. Optimal Input Features for Tree Species Classification in Central Europe Based on Multi-Temporal Sentinel-2 Data. *Remote Sensing*, 11(22), 2599, doi.org/10.3390/rs11222599.

Jarocińska, A., Kopeć, D., Niedzielko, J., Wylazłowska, J., Halladin-Dąbrowska, A., Charyton, J., Piernik, A., Kamiński, D., 2023. The utility of airborne hyperspectral and satellite multispectral images in identifying Natura 2000 non-forest habitats for conservation purposes. *Scientific Reports*, 13(1), 4549, doi.org/10.1038/s41598-023-31705-6.

Jenal, A., Kneer, C., Weber, I., Asgari, M., Knieps, M., Bongartz, J., 2022. An Adaptive Sensor Framework for Gyrocopter-Based Optical Remote Sensing: Introduction and Applications. *PFG – Journal of Photogrammetry, Remote Sensing and Geoinformation Science*, 90, 93, doi.org/10.1007/s41064-021-00187-4.

Jenal, A., Hütt, C., Reddig, F., Bolten, A., Bareth, G., Bongartz, J., 2024. Expanding Horizons: Introducing a 6-Channel VNIR-SWIR Multicamera System for Advanced UAV-based Remote Sensing Applications. Publikationen der DGPF, Band 32, doi.org/10.24407/KXP:1885709293.

Marcinkowska-Ochtyra, A., Ochtyra, A., Raczko, E., Kopeć, D., 2023. Natura 2000 Grassland Habitats Mapping Based on Spectro-Temporal Dimension of Sentinel-2 Images with Machine Learning. *Remote Sensing*, 15(5), 1388, doi.org/10.3390/rs15051388.

Martínez Prentice, R., Villoslada, M., Ward, R. D., Bergamo, T. F., Joyce, C. B., Sepp, K., 2024. Synergistic use of Sentinel-2 and UAV-derived data for plant fractional cover distribution mapping of coastal meadows with digital elevation models. Biogeosciences, 21(6), 1411–1431, doi.org/10.5194/bg-21-1411-2024.

Meerdink, S.K., Hook, S.J., Roberts, D.A., Abbott, E.A., 2019. The ECOSTRESS spectral library version 1.0. *Remote Sensing of Environment*, 230, 111196, doi.org/10.1016/j.rse.2019.05.015.

MKUEM, 2024. Kartieranleitung für die Erfassung der gesetzlich geschützten Biotope nach § 30 BNatSchG und § 15 LNatSchG in Rheinland-Pfalz. Stand: 05.03.2024. Ministerium für Klimaschutz, Umwelt, Energie und Mobilität Rheinland-Pfalz.

Rapinel, S., Mony, C., Lecoq, L., Clément, B., Thomas, A., Hubert-Moy, L., 2019. Evaluation of Sentinel-2 time-series for mapping floodplain grassland plant communities. *Remote Sensing of Environment*, 223, 115–129, doi.org/10.1016/j.rse.2019.01.018.

Reinermann, S., Asam, S., Kuenzer, C., 2022. Detection of Grassland Mowing Events for Germany by Combining Sentinel-1 and Sentinel-2 Time Series. *Remote Sensing*, 14(7), 1647, doi.org/10.3390/rs14071647

Schwieder, M., Wesemeyer, M., Frantz, D., et al., 2022. Mapping grassland mowing events across Germany based on combined Sentinel-2 and Landsat 8 time series. *Remote Sensing of Environment*, 269, 112795, doi.org/10.1016/j.rse.2021.112795.

Tarantino, C., Forte, L., Blonda, P., Vicario, S., Tomaselli, V., Beierkuhnlein, C., Adamo, M., 2021. Intra-Annual Sentinel-2 Time-Series Supporting Grassland Habitat Discrimination. *Remote Sensing*, 13(2), 277, doi.org/10.3390/rs13020277.

Vanden Borre, J., Paelinckx, D., Mücher, C. A., Kooistra, L., Haest, B., De Blust, G., Schmidt, A. M., 2011. Integrating remote sensing in Natura 2000 habitat monitoring: Prospects on the way forward. *Journal for Nature Conservation*, 19(2), 116–125, doi.org/10.1016/j.jnc.2010.07.003.

Wakulińska, M., Marcinkowska-Ochtyra, A., 2020. Multi-Temporal Sentinel-2 Data in Classification of Mountain Vegetation. Remote Sensing, 12(17), 2696, doi.org/10.3390/rs12172696.